

On reconstruction of dynamic permeability and tortuosity from data at distinct frequencies

Miao-Jung Yvonne Ou[†],

[†]Department of Mathematical Sciences, University of Delaware, Newark, DE 19716, USA,
mou@math.udel.edu

Abstract

This article focuses on the mathematical problem of reconstructing the dynamic permeability $K(\omega)$ and dynamic tortuosity of poroelastic composites from permeability data at different frequencies, utilizing the analytic structure of the Stieltjes function representation of $K(\omega)$ derived by Avellaneda and Tortquato in [7], which is valid for all pore space geometry. The integral representation formula (IRF) for dynamic tortuosity is derived and its analytic structure exploited for reconstructing the function from a finite data set. All information of pore-space microstructure is contained in the measure of the IRF. The theory of multipoint Padé approximates for Stieltjes functions guarantees the existence of relaxation kernels that can approximate the dynamic permeability function and the dynamic tortuosity function with high accuracy. In this paper, a numerical algorithm is proposed for computing the relaxation time and the corresponding strength for each element in the relaxation kernels. In the frequency domain, this approximation can be regarded as approximating the Stieltjes function by rational functions with simple poles and positive residues. The main difference between this approach and the curve fitting approach is that the relaxation times and the strengths are computed from the partial fraction decomposition of the multipoint Padé approximates, which is the main subject of the proposed approximation scheme.

With the idea from dehomogenization, we also established the exact relations between the moments of the positive measures in the IRFs of permeability and tortuosity with two important parameters in the theory of poroelasticity: the infinite-frequency tortuosity α_∞ for the general case and the weighted volume-to-surface ratio Λ for the JKD model, which is regarded as a special case of the general model. From these relations, we suggest a new way for evaluating these two microstructure-dependent parameters from a finite data set of permeability at different frequencies, without assuming any specific forms of the functions except the fact that they satisfies the IRFs. Numerical results for JKD permeability and tortuosity are presented.

Keywords: Dynamic permeability, dynamic tortuosity, poroelasticity, Stieltjes functions, multipoint Padé approximates, ill-posed problems, Tikhonov regularization, L -curve method, relaxation kernels, Biot-JKD equations, moments

1 Notations

The notations used in this paper are listed here.

- $A := B$ means A is defined by B
- $A =: B$ means A defines B
- $A \approx B$ means A is approximated by B
- Superscript D is added to parameters to denote their values in the Johnson, Koplik and Dashen (JKD) model.
- $d\lambda$ is reserved for the positive measure in the IRF of permeability functions.
- $d\sigma$ is reserved for the positive measure in the IRF of tortuosity functions.

2 Introduction

Poroelasticity theory is a homogenized model for solid porous media containing slightly compressible fluids that can flow through the pore structure. This field was pioneered by Maurice A. Biot, who developed his theory of poroelasticity from the 1930s through the 1960s; a summary of much of Biot’s work can be found in his 1956 and 1962 papers [10, 11, 12]. Biot theory uses linear elasticity to describe the solid portion of the medium (often termed the *skeleton* or *matrix*), linearized compressible fluid dynamics to describe the fluid portion, and Darcy’s law to model the aggregate motion of the fluid through the matrix. While it was originally developed to model fluid-saturated rock and soil, Biot theory has also been used in underwater acoustics [13, 36, 37], and to describe wave propagation in *in vivo* bone [24, 25, 35]. Biot’s equations have been validated mathematically through applying homogenization techniques by various authors, e.g. [17] [5, 6] [67] [38] [23]. Regularity of solutions to isotropic poroelastic equations has been studied in [60].

Biot theory predicts rich and complex wave phenomena within poroelastic materials. Three different types of waves appear: fast P waves analogous to standard elastic P waves, in which the fluid and matrix show little relative motion, and typically compress or expand in phase with each other; shear waves analogous to elastic S waves; and slow P waves, where the fluid expands while the solid contracts, or vice versa. The slow P waves exhibit substantial relative motion between the solid and fluid compared to waves of the other two types. The viscosity of the fluid dissipates poroelastic waves as they propagate through the medium, with the fast P and S waves being lightly damped and the slow P wave strongly damped. The viscous dissipation also causes slight dispersion in the fast P and S waves, and strong dispersion in the slow P wave.

A variety of different numerical approaches have been used to solve poroelastic equations. Carcione, Morency, and Santos provide a thorough review of the previous literature [18]. The earliest numerical work in poroelasticity seems to be that of Garg [33], using a finite difference method in 1D. Finite difference and pseudospectral methods have continued to be popular since then, with further work by Mikhailenko [50], Hassanzadeh [40], Dai et al. [26], and more recently Chiavassa and Lombard [22], among others. Finite element approaches began being used in the 1980s, with Santos and Oreña’s work [58] being one of the first. Boundary element methods have also been used, such as in the work of Attenborough, Berry, and Chen [4]. Spectral element methods have also been used in both the frequency domain [28] and the time domain [51]. With the recent rise of discontinuous Galerkin methods, DG has been applied to poroelasticity in several works, such as that of de la Puente et al. [27]. A Finite Volume Method solver for 2D and 3D Biot’s equations can be found in [45] and [46]. There have also been semi-analytical approaches to solving the poroelasticity equations, such as that of Detournay and Cheng [29], who analytically obtain a solution in the Laplace transform domain, but are forced to use an approximate inversion procedure to return to the time domain. Finally, there has been significant work on inverse problems in poroelasticity, for which various forward solvers have been used [59] [16]; of particular note is the paper of Buchanan, Gilbert, and Khashanah [15], who used the finite element method (specifically the FEMLAB software package) to obtain time-harmonic solutions for cancellous bone as part of an inversion scheme to estimate poroelastic material parameters, and the later papers of Buchanan and Gilbert [14], where the authors instead used numerical contour integration of the Green’s function. In [59], numerical results from Biot’s equations are compared with the experimental measurement of ultrasound propagation in cancellous bone. The physical parameters involved in the drag force are the tortuosity and the permeability.

In the Biot equations for wave propagation in poroelastic materials [10, 11], a critical frequency ω_c is defined. For frequency below ω_c , the pore fluid flow is laminar and the friction term which takes into account the viscous interaction between the solid matrix and pore fluid

is modeled by the product of friction constant and the difference between the fluid velocity and the solid velocity. We refer to this set of equations as low-frequency Biot equations. For frequency higher than ω_c , the friction constant is multiplied by a frequency-dependent function to correct for the departure from laminar flow; this leads to a memory term in the time domain Biot equations. The exact form of the memory kernel is not known except for specific pore shapes such as parallel tubes [11, 6]. This set of equations are referred to as high-frequency Biot equations.

The need for quantifying the dissipation's dependence on frequency for more general pore space geometry prompted the work in the seminal paper [43] by Johnson, Koplik and Dashen (JKD), in which the theory of dynamic fluid permeability $K^D(\omega)$ and dynamic tortuosity $T^D(\omega)$ was developed for describing the **inertial coupling** and **viscous coupling** between matrix solid and pore fluid. Using the causality argument, they derived the necessary symmetries and analytic properties of $K(\omega)$ and $T(\omega)$ when ω is extended to the complex values. Most importantly, they postulated the simplest forms of $K(\omega)$ and $T(\omega)$ which satisfy those properties. These two functions contain a tunable parameter Λ take into account of the dependence on pore space geometries. However, it is very difficult to measure and is usually calculated through the empirical formula [54] $\Lambda \approx \sqrt{\frac{2\alpha_\infty K_0}{\phi/4}}$, where α_∞ is the infinite-frequency tortuosity, K_0 the static permeability and ϕ the porosity. The problem is that it is not clear how well this formula approximates Λ and even if it does, the measurement of α_∞ is very difficult and is still an active research area [3], [30], [42], [48], [63], [31].

The Biot-JKD equations refer to the set of Biot equations modified by the JKD theory. In Biot-JKD equations no critical frequency is defined and the friction term (the drag force) is always a memory term.

Due to the numerical complexity brought by the memory terms, most time-domain (vs frequency domain) solvers in the literature consider low-frequency Biot's equations even though it is well known in geological and biological applications that low-frequency Biot equations underestimate wave dissipation when compared with experiments. There have been a few papers which proposed different methods for handling the memory terms. Among them, the most popular ones are the fractional derivative approach for Biot-JKD model, which requires complicated quadrature rules [47] and the phenomenological one which proposed to approximate the memory terms with sums of exponential decay kernels [64],[19]. The latter is more computationally efficient but it is not clear how the weights and decay rates of the exponential decay kernels can be found in a systematic way.

The aims of this paper are

1. To utilize the integral representation formula (IRF) of dynamic permeability, which is derived in [7], to develop a numerical scheme that can reconstruct the dynamic permeability function from any finite set of data measured at different frequencies. Unlike the JKD model, it does not impose any specific form on the permeability function.
2. To use the proposed numerical scheme, together with the relation between tortuosity and permeability, to reconstruct the tortuosity function from the finite data set. The weights and decay rates of the exponential decay kernel then come naturally along this process due to the mathematical structure of the tortuosity IRF derived in this paper.
3. To quantify how microstructure affects the tortuosity and other effective parameters relevant to drag force, which is known to be an important signaling mechanism for activating the cell process for bone remodeling, [56, 44, 49, 53, 55, 57].

The paper is organized as follows. In Section 3, definition of permeability and its role in the poroelastic equations, the mathematical tools essential to the derivation of the tortuosity IRF and the inversion scheme are explained. In Section 4, the numerical scheme for reconstructing permeability functions from a finite data set is presented. Numerical results for the Biot-JKD

model, which is regarded as a special case, are demonstrated. The proof that the JKD permeability function indeed can be represented as an IRF with a probability measure is also given there. In Section 5, an IRF of the dynamic tortuosity function is derived. With this IRF, we prove that the time domain dynamic tortuosity function can be approximated by a combination of the Dirac function at $t = 0$ and a sum of exponentially decay kernels whose rates and strengths can be computed from the proposed numerical scheme. Numerical results for the JKD tortuosity is demonstrated there. In Section 6, we present three exact (vs approximated) mathematical formulas which quantify how the geometry of pore space affects various effective poroelastic parameters through moments. Finally, in Section 7 we summarize the results and compare our exact formula for Λ with an existing empirical formula. Also, future work is pointed out there.

3 Mathematical Background

3.1 Permeability and Tortuosity

For a **rigid** porous medium filled with Newtonian pore fluid with density ρ_f and **dynamic** viscosity η , a key effective property is the fluid permeability tensor \mathbf{K} , which is described by the so-called Darcy's law, [6, 43, 7, 62]

$$\mathbf{U} = -\frac{\mathbf{K}}{\eta} \nabla p \quad (1)$$

where \mathbf{U} is the averaged fluid velocity over a representative volume element (RVE) of the porous medium and ∇p the applied pressure gradient; this is referred to as the **static** permeability. If the applied pressure gradient is oscillatory with frequency ω , then the induced averaged fluid velocity will also be oscillatory and proportional to $\nabla p(\omega)$ by

$$\mathbf{U}(\omega) = -\frac{\mathbf{K}(\omega)}{\eta} \nabla p(\omega) \quad (2)$$

where $\mathbf{K}(\omega)$ is referred to as the **dynamic** permeability, [43, 7]. $\mathbf{K}(\omega)$ varies with ω because the viscous interaction between fluid and solid varies with frequency, as indicated by the frequency dependent viscous skin depth $\sqrt{\frac{2\eta}{\rho_f \omega}}$. For $\omega \neq 0$ the tortuosity tensor \mathbf{T} is related to $\mathbf{K}(\omega)$ by

$$\mathbf{T}(\omega) = \frac{i\eta\phi}{\omega\rho_f} \mathbf{K}^{-1}(\omega), \quad i = \sqrt{-1} \text{ (note } \mathbf{T}(\omega) \text{ has a pole at } \omega = 0\text{)}. \quad (3)$$

As was mentioned in Section 2, there are two different forms of drag forces in Biot equations, depending on whether it is below or above the critical frequency $\omega_c := \frac{\phi\eta}{\rho_f \alpha_\infty K_0}$, $K_0 := K(0)$, [20]; for a low frequency, in the frequency domain, the drag force is $b \times$ (fluid velocity relative to solid velocity) with $b = \eta\phi^2/K_0$, whereas for a high frequency, the constant b is replaced by $b \cdot F(\omega)$ where $Im(F(\omega)) \rightarrow 0$ and $Re(F(\omega)) \rightarrow 1$ as $\omega \rightarrow 0$. Biot derived the exact expression of $F(\omega)$ for thin circular tubes in terms of zero-order Kelvin functions of the first kind, [10] and assumed the same functional form for all other pore geometry by a heuristically defined correction constant. In [43], the Biot-JKD equations are proposed by unifying the two types of friction terms in Biot's equations with a frequency-dependent function. For isotropic poroelastic materials, based on physics-based argument and exact calculation of parallel circular tubes, Johnson, Koplik and Dashen postulated the isotropic dynamic tortuosity to be of the form

$$T^D(\omega) = \alpha_\infty \left(1 - \frac{\eta\phi}{i\omega\alpha_\infty\rho_f K_0} \sqrt{1 - i \frac{4\alpha_\infty^2 K_0^2 \rho_f \omega}{\eta \Lambda^2 \phi^2}} \right) =: \alpha(\omega) \quad (4)$$

with the tunable geometry-dependent constant Λ , and (3) implies

$$K^D(\omega) = K_0 / \left(\sqrt{1 - \frac{4i\alpha_\infty^2 K_0^2 \rho_f \omega}{\eta \Lambda^2 \phi^2}} - \frac{i\alpha_\infty K_0 \rho_f \omega}{\eta \phi} \right). \quad (5)$$

, where $\eta = \rho_f \nu$ is the dynamic viscosity of pore fluid.

The homogenization analysis in [6] and physical arguments in [43] shows that the permeability in Biot(-JKD) equations for poroelastic materials is identical to that for porous media with a rigid matrix. Furthermore, the permeability can be mathematically characterized as a functional of the solution to the unsteady Stokes equation, [7]

$$\frac{\partial \mathbf{v}}{\partial t} = -\nabla \left(\frac{p}{\rho_f} \right) + \nu \Delta \mathbf{v} + v_0 \mathbf{e} \delta(t) \text{ in } \mathcal{V}_1, \quad \nabla \cdot \mathbf{v} = 0 \text{ in } \mathcal{V}_1, \quad \mathbf{v} = \mathbf{0} \text{ on } \partial \mathcal{V} \quad (6)$$

where \mathbf{e} is an arbitrary unit vector if \mathbf{K} is statistically isotropic, v_0 a constant, ν the **kinetic** viscosity, $\delta(t)$ the Dirac delta function, \mathcal{V}_1 the region occupied by pore fluid and $\partial \mathcal{V}$ is the interface between fluid phase and solid phase in the RVE with periodic condition (or statistically homogeneous in the random media setting) on the outer boundary of RVE. As is indicated in [7], the results can be easily generalized to all statistically homogeneous anisotropic \mathbf{K} . However, we assume \mathbf{K} is isotropic in this paper for simplicity. It is shown in [7] the solution $\mathbf{v}(\mathbf{x}, t)$ can be expressed as a sum of the normal modes Ψ_n

$$\mathbf{v}(\mathbf{x}, t) = v_0 \sum_{n=1}^{\infty} b_n e^{-t/\Theta_n} \Psi_n(\mathbf{x}) \quad (7)$$

where Ψ_n are the eigenfunctions of the Stokes system

$$\Delta \Psi_n + \nabla Q_n = -\epsilon_n \Psi_n \text{ and } \nabla \cdot \Psi_n = 0 \text{ in } \mathcal{V}_1, \quad \Psi_n = 0 \text{ on } \partial \mathcal{V}_1, \quad \Theta_n := (\nu \epsilon_n)^{-1} \quad (8)$$

$0 < \epsilon_1 \leq \epsilon_2 \leq \dots$ and $\epsilon_n \rightarrow \infty$ as $n \rightarrow \infty$. Θ_n are the viscous relaxation times and Θ_1 referred to as the principal viscous relaxation time. The eigenfunctions are orthonormal in the sense

$$\frac{1}{|\mathcal{V}_1|} \int_{\mathcal{V}_1} \Psi_m(\mathbf{x}) \cdot \Psi_n(\mathbf{x}) d\mathbf{x} = \delta_{mn} \text{ (Kronecker delta)} \quad (9)$$

and the b_n in (7)

$$b_n = \frac{1}{|\mathcal{V}_1|} \int_{\mathcal{V}_1} \mathbf{e} \cdot \Psi_n(\mathbf{x}) d\mathbf{x} \quad (10)$$

In [7] it is shown through the classical Hodge decomposition argument that the infinite-frequency tortuosity α_∞ can be mathematically expressed as

$$\alpha_\infty = \phi F = \left(\sum_{n=1}^{\infty} b_n^2 \right)^{-1} \quad (11)$$

This shows the microstructure information affects α_∞ through the projection of the applied flow direction on the normal modes of the Stokes equation in the pore space.

3.2 Darcy's Laws in Poroelastic Equations and Permeability IRF

The state variables for both Biot and Biot-JKD equations are \mathbf{v} (solid velocity), \mathbf{q} (fluid velocity relative to the solid) and p (pore pressure). Note that \mathbf{v} and p have different meanings from before and will stay unchanged hereafter. The stress-velocity formulation of Biot-JKD equations

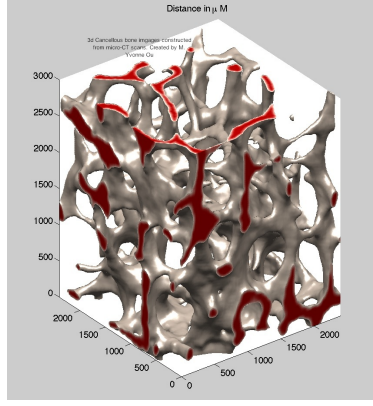


Figure 1: Cancellous bone, M.Y. Ou and L. Cardoso 2012

in a plane-strain case consists of

$$\partial_t \tau_{xx} = c_{11}^u \partial_x v_x + c_{13}^u \partial_z v_z + \alpha_1 M (\partial_x q_x + \partial_z q_z) + \partial_t s_1 \quad (12)$$

$$\partial_t \tau_{zz} = c_{13}^u \partial_x v_x + c_{33}^u \partial_z v_z + \alpha_3 M (\partial_x q_x + \partial_z q_z) + \partial_t s_3 \quad (13)$$

$$\partial_t \tau_{xz} = c_{55}^u (\partial_z v_x + \partial_x v_z) + \partial_t s_5 \quad (14)$$

$$\partial_t p = -\alpha_1 M \partial_x v_x - \alpha_3 M \partial_z v_z - M (\partial_x q_x + \partial_z q_z) + \partial_t s_f, \quad (15)$$

$$\rho \partial_t v_x + \rho_f \partial_t q_x = \partial_x \tau_{xx} + \partial_z \tau_{xz} \quad (16)$$

$$\rho \partial_t v_z + \rho_f \partial_t q_z = \partial_x \tau_{xz} + \partial_z \tau_{zz} \quad (17)$$

and the Darcy's laws which are the inverse Fourier transform of the following equation

$$-\nabla \tilde{p} = \eta \phi \mathbf{K}^{-1} \tilde{\mathbf{q}} + \rho_f (-i\omega) \tilde{\mathbf{v}}_s = -i\omega \frac{\rho_f}{\phi} \mathbf{T}^D(\omega) \tilde{\mathbf{q}} + \rho_f (-i\omega) \tilde{\mathbf{v}}_s \quad (18)$$

where $\tilde{\mathbf{q}}$, $\tilde{\mathbf{v}}_s$, \tilde{p} are Fourier transforms of \mathbf{q} , \mathbf{v} and p , respectively. The Fourier transform we use here is

$$\mathcal{F}[f](\omega) = \tilde{f}(\omega) := \frac{1}{\sqrt{2\pi}} \int_0^\infty f(t) e^{i\omega t} dt$$

The real part of \mathbf{K}^{-1} corresponds to the dissipation term and the imaginary part to the inertial term in the time domain where the drag force is expressed as a time-convolution term, [6, 47]. The complete form of any component of $\mathbf{K}(\omega)$ for all ω is very difficult to compute for a given porous medium such as cancellous bone, whose pore geometry is complicated, see Fig. 1. Hereafter, we consider isotropic \mathbf{K} and hence replace \mathbf{K} with K . It is pointed out in [43] that when $\alpha(\omega)$ and $K(\omega)$ are extended to the complex ω -plane, they are analytic in the upper half plane because of causality and have the symmetry property $\alpha(-\bar{\omega}) = \overline{\alpha(\omega)}$ and $K(-\bar{\omega}) = \overline{K(\omega)}$, where the bar means complex conjugation. It is remarkable that in [7] $K(\omega)$ is derived rigorously for **all** pore space geometries as a Stieltjes integral with distribution $G(\Theta)$ that is nondecreasing, right-continuous, $G(\Theta) = 0$ for $\Theta \leq 0$ and $G(\Theta) = 1$ for $\Theta \geq \Theta_1$ (i.e., a probability distribution) such that

$$\left(\frac{F}{\nu}\right) K(\omega) = \int_0^\infty \frac{\Theta dG(\Theta)}{1 - i\omega\Theta}, \text{ with } G(\Theta) = \frac{\sum_{\Theta_n \leq \Theta} b_n^2}{\sum_{n=1}^\infty b_n^2}. \quad (19)$$

The derivation is based on identifying the exact functional form of $K(s)$ in terms of the solution to the Laplace transformed equations of (6) with the parameter $s = -i\omega$.

3.3 Stieltjes functions and Multipoint Padé approximation

The reconstruction scheme proposed in this paper is based on the properties of N -point approximation for Stieltjes functions. Two different but related definitions of Stieltjes functions are widely used in the literature, we adopt the following definition in this paper.

Definition 3.1. A Stieltjes function $f(z)$ for z on the extended complex plane has the following form

$$f(z) = \int_a^b \frac{d\mu(t)}{z-t} \quad (20)$$

where a, b are extended real numbers and $\mu(t)$ is a bounded, non-decreasing real function.

A multipoint Padé approximation of a function f is a rational function interpolating f at various points, not necessarily distinct. The following theorem (Theorem 1 on p. 26 of [34]) is the foundation of the reconstruction algorithm proposed in this paper and hence we state it here.

Theorem 3.1 ([34]). Suppose f is a Stieltjes function of the form in (20). Let $P_{n-1}(z)$ and $Q_n(z)$ be polynomials of degree at most $n-1$ and n , respectively, satisfying the relations $(k_1 + k_2 + k_3 = 2n)$

$$\begin{cases} f(z)Q_n(z) - P_{n-1}(z) = A(z)(z-x_1)\cdots(z-x_{k_1})(z-z_1)(z-\bar{z}_1)\cdots(z-z_{k_2})(z-\bar{z}_{k_2}) \\ f(z)Q_n(z) - P_{n-1}(z) = B(z)z^{n-k_3-1} \end{cases}$$

where $A(z), B(z)$ are analytic in $\mathbb{C} \setminus [a, b]$, $B(z)$ bounded at ∞ , $x_1, \dots, x_{k_1} \in \mathbb{R} \setminus [a, b]$, $z_1, \dots, z_{k_2} \in \mathbb{C} \setminus \mathbb{R}$. Then $\frac{P_{n-1}(z)}{Q_n(z)} = \int_a^b \frac{d\beta(t)}{z-t}$ for some bounded, non-decreasing function $\beta(t)$.

Here $[n-1/n]_f(z) := \frac{P_{n-1}(z)}{Q_n(z)}$ is referred to as the $2n$ -point Padé approximant for f and is unique [34]. It has nice convergent properties in $\mathbb{C} \setminus [a, b]$ as long as the interpolating points are of the types specified in the theorem above. The significance of Theorem 3.1 is that when the complex-valued interpolating points appear in conjugate pairs, the approximant of a Stieltjes function can be expressed as

$$[n-1/n]_f(z) = \sum_{k=1}^n \frac{r_k}{z-p_k} \quad (21)$$

with $r_k > 0$ and $p_k \in (a, b)$ for $k = 1, \dots, n$. It will be made clear later in the paper that this property can be used for generating efficient quadrature rules for dealing with the memory term in the dynamic Darcy's law (18) in time domain.

4 Reconstruction of Dynamic Permeability

Our experience with dehomogenization indicates that $K(\omega)$ can be reconstructed with a very good accuracy from partial data by exploring its mathematical structure as a Stieltjes function, [21, 65, 66]. Define a new variable s and a new function $P(s)$

$$s := -i\omega, \quad P(s) := \left(\frac{F}{\nu}\right) K(is) = \int_0^{\Theta_1} \frac{\Theta dG(\Theta)}{1+s\Theta} =: \int_0^{\Theta_1} \frac{d\lambda(\Theta)}{1+s\Theta} \quad (22)$$

$$\xi := -1/s, \quad R(\xi) := -s \left(\frac{F}{\nu}\right) K(is) = -sP(s) = \int_0^{\Theta_1} \frac{\Theta dG(\Theta)}{\xi - \Theta}. \quad (23)$$

We summarize the definitions of auxiliary variables and auxiliary functions in Table 1.

It is clear that $R(\xi)$ in (23) is a Stieltjes function with. Due to the IRF of $P(s)$ in (22), it is known that its Padé approximants have accuracy-through-order property [8], and all the

ω	$s := -i\omega$	$\xi := -\frac{1}{s}$
$K(\omega)$	$P(s) := (\frac{F}{\nu}) K(is)$	$R(\xi) := -sP(s)$

Table 1: Auxiliary variables and functions for dynamic permeability $K(\omega)$

poles of the Padé approximants are simple with positive residue in $[-\infty, -\frac{1}{\Theta_1}]$ on the complex s -plane [52]. Most importantly, the Multipoint Padé approximants (or rational interpolants) with interpolation knots $\{s_k\}_{k=1}^N$ with either $s_k > 0$ or conjugate complex numbers appearing in pairs has interlacing simple zeros and simple poles locating in the regions where $P(s)$ is not analytic [61]. Suppose we have values of $K(\omega_j)$ for different nonzero frequencies $\omega_1, \omega_2, \dots, \omega_M \in \mathbb{R}$. This means the values of $R(\xi)$ for $\xi_k = \frac{-i}{\omega_k} \in \mathbb{C} \setminus \mathbb{R}$, $k = 1, \dots, M$ are known. To generate the complex conjugated interpolating points at $\bar{\xi}_k$, we note that (23) implies

$$R(\bar{\xi}) = \int_0^{\Theta_1} \frac{\theta dG(\theta)}{\bar{\xi} - \theta} = \overline{\int_0^{\Theta_1} \frac{\theta dG(\theta)}{\xi - \theta}} = \overline{R(\xi)}$$

because $\theta, G(\theta) \in \mathbb{R}$. Hence the data of K at M different frequencies indeed provide $2M$ data points for the reconstruction of R through this symmetry. The $2M$ -point Padé approximants are formulated as follows.

$$R(\xi_j) = \int_0^{\Theta_1} \frac{\Theta dG(\Theta)}{\xi_j - \Theta} \approx [M - 1/M]_R(\xi) := \frac{a_0 + a_1\xi_j + \dots + a_{M-1}\xi_j^{M-1}}{1 + b_1\xi_j + \dots + b_M\xi_j^M}, j = 1, \dots, 2M \quad (24)$$

We know that the constant term in the denominator can be normalized to 1 and the unknowns $a_0, \dots, a_{M-1}, b_1, \dots, b_M$ can be assumed real-valued because of (21). Furthermore, the moments of dG can be computed from partial fraction decomposition of it when lower frequency data points are used. Note that the first-moment of dG is equal to $\frac{FK_0}{\nu}$ and hence the formation factor $F := \frac{\alpha_\infty}{\phi}$ can be recovered from the numerically estimated moments if K_0 and ν are known. That is, the tortuosity α_∞ can be recovered from data of $K(\omega)$ at low frequencies if the porosity ϕ is known. In terms of the partial fraction decomposition of $[M - 1/M]_R(\xi)$

$$[M - 1/M]_R(\xi) = \sum_{j=1}^M \frac{r_j}{\xi - p_j}, r_j > 0, 0 < p_j < \Theta_1 \quad (25)$$

the approximation of dynamic permeability K can be expressed as

$$K(\omega) \approx \frac{\nu}{F} \sum_{j=1}^M \frac{r_j}{1 - i\omega p_j} \quad (26)$$

Therefore, the permeability in time domain can be approximated as

$$\mathcal{F}^{-1}[K](t) = \left(\frac{\nu}{F}\right) \sum_{j=1}^M \left(\frac{r_j}{p_j}\right) e^{-\frac{t}{p_j}} \quad (27)$$

4.1 Formulation and Algorithm

For better conditioning of the inversion scheme, the reconstruction is based on (38), rather than $R(\xi)$.

Suppose we have values of $K(\omega_j) = K(is_j) = P(s_j)$ for different nonzero real-valued frequencies $\omega_1, \omega_2, \dots, \omega_M$, then we can generate another M -interpolation points by using the symmetry of (19) for $\omega \in \mathbb{R}$

$$\left(\frac{F}{\nu}\right) P(\bar{s}_j) = K(-\omega_j) = K(-\bar{\omega}_j) = \overline{K(\omega_j)} = \left(\frac{F}{\nu}\right) \overline{P(s_j)}, j = 1, \dots, 2M.$$

Because of (25) and (26), we can approximate $P(s)$ as

$$P(s_j) = \int_0^{\Theta_1} \frac{\Theta dG(\Theta)}{1 + s_j \Theta} \approx [M - 1/M]_P(s) := \frac{a_0 + a_1 s_j + \dots + a_{M-1} s_j^{M-1}}{1 + b_1 s_j + \dots + b_M s_j^M}, j = 1, 2, \dots, 2M \quad (28)$$

and the moments of dG can be computed from partial fraction decomposition of the approximant when lower frequency data are used. We know that the constant term in the denominator can be normalized to 1 because all the poles are simple and located in $(-\infty, -\frac{1}{\Theta_1})$.

Given the data $(s_j, P(s_j))$, $s_j \neq 0$, $j = 1, \dots, M$, let $s_{j+M} = \bar{s}_j$, $P(s_{j+M}) = \overline{P(s_j)}$ and $P_m := P(s_m)$, $m = 1, \dots, 2M$, then (28) leads to the linear system of equations $Ax = d$,

$$\begin{aligned} A &= \begin{pmatrix} 1 & s_1 & s_1^2 & \dots & s_1^{M-1} & -P_1 s_1 & -P_1 s_1^2 & -P_1 s_1^3 & \dots & -P_1 s_1^M \\ 1 & s_2 & s_2^2 & \dots & s_2^{M-1} & -P_2 s_2 & -P_2 s_2^2 & -P_2 s_2^3 & \dots & -P_2 s_2^M \\ \vdots & \vdots & \vdots & \vdots & \vdots & \vdots & \vdots & \vdots & \vdots & \vdots \\ 1 & s_{2M} & s_{2M}^2 & \dots & s_{2M}^{M-1} & -P_{2M} s_{2M} & -P_{2M} s_{2M}^2 & -P_{2M} s_{2M}^3 & \dots & -P_{2M} s_{2M}^M \end{pmatrix} \\ &= A_r + i A_i, \\ \mathbf{x} &= (a_0, a_1, \dots, a_{M-1}, b_1, b_2, \dots, b_M), \\ \mathbf{d} &= (P_1 \ P_2 \ \dots \ P_{2M})^t \end{aligned} \quad (29)$$

where A_r and A_i are the real part and imaginary part of A , respectively. Since multi-point Padé approximants of $P(s)$ constructed in this way have real-valued simple poles p_j with positive residues r_j , $j = 1, \dots, N$, we have

$$[M - 1/M]_P(s) := \frac{a_0 + a_1 s + \dots + a_{M-1} s^{M-1}}{1 + b_1 s + \dots + b_M s^M} = \sum_{j=1}^M \frac{r_j}{s - p_j}$$

and $\mathbf{x} \in \mathbb{R}^{2M}$. Noting that we have $2M$ real-valued unknowns and $2M$ complex-valued data for the linear system with complex coefficients, there are $4M$ equations with real-valued coefficients for the $2M$ real-valued unknowns. Rather than solving the formal equations of $Ax = d$ as in [65, 66] in least-square sense, which requires forming $A_r^t A_r$ and $A_i^t A_i$, we solve this system of equations as an overdetermined least square problem by the following algorithm

1. Rescale each column \mathbf{a}_j , $j = 1, \dots, 2M$ of A by $C := \text{diag}\{\|\mathbf{a}_j\|_2^{-1}\}_{j=1}^{2M}$. Let

$$A\mathbf{x} = (AC)(C^{-1}\mathbf{x}) =: B\mathbf{y}$$

2. Let

$$\hat{B} := \begin{pmatrix} B_r \\ B_i \end{pmatrix}, \hat{\mathbf{d}} := \begin{pmatrix} \mathbf{d}_r \\ \mathbf{d}_i \end{pmatrix}. \quad (30)$$

Solve the overdetermined system $\hat{B}\mathbf{y} = \hat{\mathbf{d}}$ in the least square sense with Tikhonov regularization

$$\min_{\mathbf{y}} \|\hat{B}\mathbf{y} - \hat{\mathbf{d}}\|_2^2 + \gamma^2 \|\mathbf{y}\|_2^2$$

The L -curve method [39] is used for choosing the regularization parameter γ

3. Rescale $\mathbf{x} = C\mathbf{y}$.
4. Apply partial fraction decomposition to the resulting $2M$ -point Padé approximant. Retain only the negative poles in $(-\infty, -\frac{1}{C_1}] \cup \{-\frac{1}{\xi_p}\}$ with positive weights and discard the rest.

Theoretically, all the poles in Step 4 should be in the range specified there. Numerically, the ill-posed nature of the inverse problem leads to poles outside the range. Suppose M' poles are retained after discarding the spurious poles, $M' \leq M$, we reindex them and the corresponding residues to $\{(p_j, r_j)\}_{j=1}^{M'}$. The function $P(s)$ is then approximated by

$$P(s) \approx P_{est}^M(s) := \sum_{j=1}^{M'} \frac{r_j}{s - p_j} = \sum_{j=1}^{M'} \frac{-r_j/p_j}{1 + s(-1/p_j)} \quad (31)$$

and the moments $\mu_k, k = 0, 1, 2, \dots$ by

$$\mu_k \approx (-1)^{k+1} \sum_{j=1}^{M'} \frac{r_j}{(p_j)^{k+1}}. \quad (32)$$

In terms of the poles and residues in (31), the time-domain permeability can be approximated by the relaxation kernel for $t \geq 0$

$$\mathcal{F}^{-1}\{K\}(t) \approx \left(\frac{\nu}{F}\right) \sum_{j=1}^{M'} r_j e^{p_j t}, \quad r_j > 0, p_j < 0.$$

Before testing the idea on the JKD permeability, we have to verify that it is consistent with the general theory presented in [7].

4.2 IRF for JKD Permeability

Since the JKD permeability in (5) was derived by a completely different approach from that in [7], we need to show K^D indeed assumes a representation of the form in (19). To see this, consider the auxiliary functions defined in Table 1 for K^D ,

$$R^D(\xi) := \frac{C_2}{\sqrt{\xi(\xi - C_1) - C_2}}, \quad C_2 := \frac{FK_0}{\nu} > 0, \quad C_1 := \frac{4C_2FK_0}{\Lambda^2} > 0, \quad (33)$$

and

$$P^D(s) := \left(\frac{F}{\nu}\right) K(is) = \left(\frac{F}{\nu}\right) \frac{K_0}{\sqrt{1 + C_1 s + C_2 s}}$$

For R^D to assume the IRF, a specific branch of the square-root function has to be chosen so $R^D(\xi)$ has all the properties implied by the integral representation. The following branch for the square root function is chosen such that the branch cut of R^D is contained in $[0, C_1], [1]$

$$R^D(\xi) = (r_1 r_2)^{1/2} e^{i(\theta_1 + \theta_2)/2} \quad (34)$$

where (r_1, θ_1) and (r_2, θ_2) are the local polar coordinates at the branch points $\xi = 0$ and $\xi = C_1$

$$\xi = r_1 e^{i\theta_1}, \quad \xi - C_1 = r_2 e^{i\theta_2}, \quad 0 \leq \theta_1, \theta_2 < 2\pi \quad (35)$$

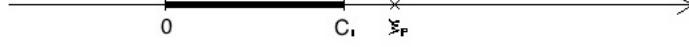


Figure 2: Branch cut and pole of R^D on the complex ξ -plane

With the chosen branch, the singular points of $R^D(\xi)$ consist of the branch cut $[0, C_1]$ and a simple pole at ξ_p , which is

$$\xi_p = \frac{C_1 + \sqrt{C_1^2 + 4C_2^2}}{2} > C_1 \quad (36)$$

See Figure ??.

We would like to remark that

1. $-R^D(\xi)$ is analytic outside $[0, \xi_p]$
2. $-R^D(\xi)$ maps the upper half plane to upper half plane with this choice of branch.
3. There exists $\kappa > 0$ such that $|yR^D(iy)| < \kappa$ for all $y > 0$ because $|yR^D(iy)| \rightarrow K_0$ as $\mathbb{R}^+ \ni y \rightarrow \infty$ and $|yR^D(iy)| \rightarrow 0$ as $\mathbb{R}^+ \ni y \rightarrow 0$.

By a general representation theorem in function theory [2], these three properties imply there exists a non-decreasing function $\lambda^D(u)$ of bounded variation on $[0, \xi_p]$ such that

$$R^D(\xi) = \int_0^{\xi_p} \frac{d\lambda^D(u)}{\xi - u} \text{ for } \xi \in \mathbb{C} \setminus [0, \xi_p]. \quad (37)$$

Transforming (37) back to $K^D(i\omega)$, we see that K^D indeed can be represented as an IRF with positive measure $d\lambda^D$

$$\frac{F}{\nu} K^D(\omega) = \int_0^{\xi_p} \frac{d\lambda^D(u)}{1 - i\omega u} \quad (38)$$

Moreover, the IRF in (23) gives additional information in the sense that it characterizes $d\lambda^D(u)$ as $udG(u)$ with dG being a probability measure. To verify this, we compute $d\lambda^D$ explicitly as follows.

Since a function of bounded variation can only have jump discontinuities and is differentiable almost everywhere, $\lambda^D(u)$ must be continuous in the support of $\lambda^D(u)$ that corresponds to the branch cut of R^D . Using the Stieltjes inversion formula on page 224 of [2], the density of $d\lambda^D$ in $[0, C_1]$ is

$$\psi(\xi) := \frac{d\lambda}{du}(\xi) = -\frac{1}{\pi} \lim_{y \rightarrow 0^+} \text{Im} R(\xi + iy) = \frac{C_2 \sqrt{\xi(C_1 - \xi)}}{\pi [C_2^2 + \xi(C_1 - \xi)]} \quad (39)$$

The pole of R^D at $\xi = \xi_p$ corresponds to a Dirac measure of $d\lambda$ at ξ_p , whose strength r can be computed from the following relation

$$R^D(\xi) = \int_0^{C_1} \frac{\psi(u)du}{\xi - u} + \frac{r}{\xi - \xi_p}$$

$$r = \lim_{\xi \rightarrow \xi_p} \left[R^D(\xi) - \int_0^{C_1} \frac{\psi(u)du}{\xi - u} \right] (\xi - \xi_p) = \lim_{\xi \rightarrow \xi_p} R^D(\xi)(\xi - \xi_p) = \frac{2C_2 \sqrt{\xi_p(\xi_p - C_1)}}{2\xi_p - C_1} \quad (40)$$

i.e.

$$d\lambda^D(u) = \chi_{\mathcal{I}}(u)\psi(u)du + r\delta_{\xi_p},$$

where $\chi_{\mathcal{I}}$ is the characteristic function of the interval $[0, C_1]$, du the Lebesgue measure and δ the Dirac measure. The following relation can be checked analytically

$$\int_0^{\xi_p} \frac{d\lambda^D(u)}{u} du = \int_0^{C_1} \frac{\psi(u)}{u} du + \frac{r}{\xi_p} = \frac{C_1}{\sqrt{C_1^2 + 4C_2^2}} + \frac{4C_2^2}{\sqrt{C_1^2 + 4C_2^2}(C_1 + \sqrt{C_1^2 + 4C_2^2})} = 1 \quad (41)$$

Our results of the JKD permeability IRF are summarized in the following theorem.

Theorem 4.1. *The JKD permeability in (5) can be represented as*

$$K^D(\omega) = \frac{\nu}{F} \int_0^{\xi_p} \frac{udG(u)}{1 - i\omega u}$$

where the probability measure dG is

$$dG(u) = \chi_{\mathcal{I}}(u) \left(\frac{\psi(u)}{u} \right) du + \left(\frac{r}{\xi_p} \right) \delta_{\xi_p},$$

with ξ_p , ψ and r defined in (36), (39) and (40), respectively.

4.3 Numerical results for $K^D(\omega)$

We use the JKD permeability function given in (5) to demonstrate the idea.

$$P^D(s) = \frac{C_2}{C_2 s + \sqrt{1 + C_1 s}} = \int_0^{\xi_p} \frac{d\lambda^D(u)}{1 + su} \quad (42)$$

implies a specific branch of the square-root function has to be chosen so P^D has all the properties implied by the integral representation such as

- It maps $Im(s) > 0$ to $Im(P(s)) < 0$.
- Its singularities are contained in $(-\infty, -\frac{1}{\Theta_1})$ for some $\Theta_1 > 0$.

We chose the branch with

$$1 + C_1 s = C_1 \left(s - \left(-\frac{1}{C_1} \right) \right) = r e^{i\theta}, r = |1 + C_1 s| \text{ and } -\pi \leq \theta < \pi$$

and

$$\sqrt{1 + C_1 s} = \sqrt{r} e^{i\theta/2}$$

with branch cut at $(-\infty, -\frac{1}{C_1})$. With this choice of branch, it can be verified that

1. $P^D(s)$ is analytic outside $(-\infty, -\frac{1}{C_1}] \cup \{ \frac{C_1 - \sqrt{C_1^2 + 4C_2^2}}{2C_2^2} = \frac{-1}{\xi_p} \}$.
2. $P^D(s)$ maps the upper half plane to lower half plane.

Table 2: Parameters used in numerical simulations.

ϕ	α_∞	$K_0(m^2)$	$\nu = \eta/\rho_f$	$\Lambda(m)$	F	C_2	C_1
0.67	1.08	7×10^{-9}	$\frac{30 \times 10^{-3} Kg/(m \cdot s)}{1060 Kg/m^3}$	10^{-5}	α_∞/ϕ	$\frac{FK_0}{\nu}$	$\frac{4C_2 FK_0}{\Lambda^2}$

Table 3: Moments of $d\lambda^D$ from data of $\omega \in [1, 51]$ Hz.

	Exact	$M = 10$	$M = 8$	$M = 6$	$M = 4$
M'		9	7	5	3
μ_0	0.3986866 e-3	0.3986865 e-3	0.3986831 e-3	0.3985660 e-3	0.3951767 e-3
μ_1	0.3602968 e-4	0.3602966 e-4	0.3602864 e-4	0.3598232 e-4	0.3469776 e-4
μ_2	0.4869721 e-5	0.4869696 e-5	0.4868684 e-5	0.4837053 e-5	0.4286249 e-5
μ_3	0.7310984 e-6	0.7310788 e-6	0.7304975 e-6	0.7173481 e-6	0.5624193 e-6
μ_4	0.1152294. e-6	0.1152184. e-6	0.1149672 e-6	0.1107076 e-6	0.7486713 e-7
μ_5	0.1867826 e-7	0.1867329 e-7	0.1858360 e-7	0.1740639 e-7	0.1000334 e-7
μ_6	0.3083493 e-8	0.3081572 e-8	0.3053660 e-8	0.2761889 e-8	0.1337903 e-8
μ_7	0.5156154 e-9	0.5149587 e-9	0.5071242 e-9	0.4402349 e-9	0.1789848 e-9
μ_8	0.8704482 e-10	0.8684085 e-10	0.8481019 e-10	0.7033276 e-10	0.2394621 e-10
μ_9	0.1480291 e-10	0.1474427 e-10	0.1424991 e-10	0.1124946 e-10	0.3203798 e-11

The exact values of the moments of $d\lambda^D$ can be computed by differentiating (42) near $s = 0$ and equating the coefficients on both sides.

$$\mu_k := \int_0^{\xi_p} u^k d\lambda^D(u) = (-1)^k \frac{P^{(k)}(0)}{k!} \quad (43)$$

The JKD-Biot parameters of cancellous bone taken from literature [24, 41, 32]: $\phi = 0.67$, $\alpha_\infty = 1.08$, $K_0 = 7 \times 10^{-9} \text{ m}^2$, $\nu = \eta/\rho_f = \frac{30 \times 10^{-3} \text{ Kg}/(\text{m} \cdot \text{s})}{1060 \text{ Kg}/\text{m}^3}$, $\Lambda = 10^{-5} \text{ m}$, $F = \alpha_\infty/\phi$. This corresponds to $C_1 = 0.17994$, $C_2 = 3.98687 \times 10^{-4}$, $-\frac{1}{C_1} = -5.55726$ and $-\frac{1}{\xi_p} = -5.55724$.

We first demonstrate the results in lower frequency range, when the reconstruction of moments is of interest. For ω between 1 Hz and 51 Hz, let $M = 4, 6, 8, 10$. For each fixed M , the frequency range $[1, 51]$ are equally divided into $M - 1$ intervals with sample frequency taken at $\omega_0 = 1$, $\omega_2 = 1 + \delta\omega, \dots, \omega_M = 51$ with $\delta\omega = 50/(M - 1)$. The corresponding moments computed from (32), together with the exact moments are listed in Table 3. The plot of these moments estimated with various values of M is in Figure 3.

Figure 4 shows the max. relative error of estimating $P(s)$ with P_M^{est} in (31), where the maximum is taken among 1000 equally spaced sample points. The maximum relative error E_∞ is defined as follows.

$$E_\infty(P_{est}^M) := \max_{s \in [-i\omega_{min}, -i\omega_{max}]} \frac{|P(s) - P_{est}^M(s)|}{|P(s)|}$$

The second example is in the range from 0.75 MHz to 4 MHz, which is the spectrum range of the incident ultrasound wave used in [32] for studying cancellous bones. $E_\infty(P_{est}^M)$ with respect to the exact P , which is P^D is shown in Figure 4. From data in this high frequency range, the moments are not well-approximated. However, it is interesting to note that the sum of residuals $\sum_{j=1}^{M'} r_j$, which serves as approximation to $\int_0^{\xi_p} \frac{d\lambda(u)}{u}$ are close to 1, as predicted by Theorem 4.1.

Examples 3 and 4 are taken from the spectral content of the incident waves used in [47] for seismic wave modeling, where the memory term is handled by the shifted fractional derivative approach. In example 3, the frequency range is from 0 to 4 kHz while the range from 4 kHz to 180 kHz is considered in example 4. Due to the wide spreading of the frequency range, the reconstruction is not as efficient as the previous two cases. However, we note that a common feature in these two cases is that the increase in E_∞ is due to the error in the frequency from

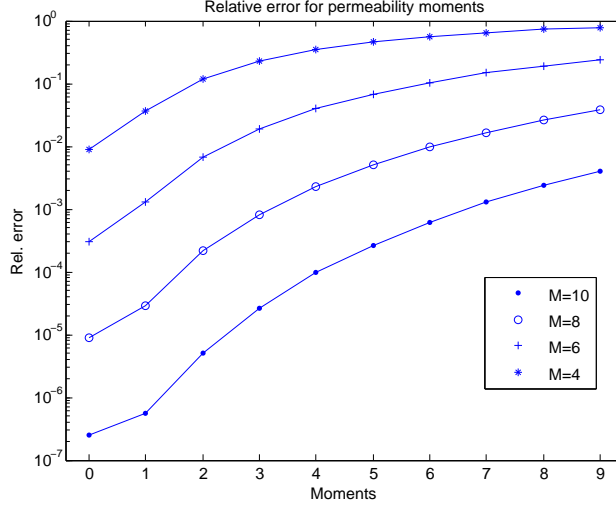


Figure 3: Relative error of $\mu_1(d\lambda^D), \dots, \mu_9(d\lambda^D)$ approximated from M data points

ω_{min} to $\omega_{min} + \delta\omega$, i.e. between the first and the second sample points in the multipoint Padé approximation. Improvement can be achieved by modifying the location of sample points. For example, in Figure 5, the curve marked by red crosses is from equally spaced sample points for $M = 10$, $\omega_{min} = 40$ Hz, $\omega_{max} = 4000$ Hz and $\delta\omega = 440$ Hz, from which the value at $\omega = 0$ can be approximated with relative error $1e-3$; excluding the first interval, the maximum relative error drops from $6.25e-2$ to $1.43e-4$.

Noting that the relative error peaks around $\delta\omega/10$ from the minimum frequency, we use 9 equally spaced sample points in the frequency range, which corresponds to $\delta\omega = 500$, and an **extra** sample point at $\omega_{min} + \delta\omega/10$. The relative error from the modified approach is marked by blue triangles in Figure 5. As indicated by (M) in Figure 6 and Figure 7, this modification brings down $E_\infty(P_{est}^M)$. The curve marked by (R) is from equally spaced sample points.

5 Reconstruction of dynamic tortuosity

In the simulation of high-frequency wave propagation in poroelastic media, the time domain Darcy's laws that come from inverse Fourier transform of (18) are part of the first-order formulation of balance law. To deal with the memory term, in [19] a phenomenological approach using generalized Zener kernels was proposed, yet not implemented, with relaxation times obtained by curve fitting. In this section, we show that the analytical structure of tortuosity T in frequency domain can be utilized to calculate the parameters needed in the dissipation kernels from a finite data set of $T(\omega_j)$, $j = 1, \dots, M$.

5.1 IRF for dynamic tortuosity $T(\omega)$

We first note that (3) implies

$$T(\omega) = - \left(\frac{\eta\phi F}{\rho_f \nu} \right) \left(\frac{1}{R(\xi)} \right) = - \frac{\alpha_\infty}{R(\xi)} \quad (44)$$

To derive the IRF, we embed $R(\xi)$ into a larger class \mathcal{S} .

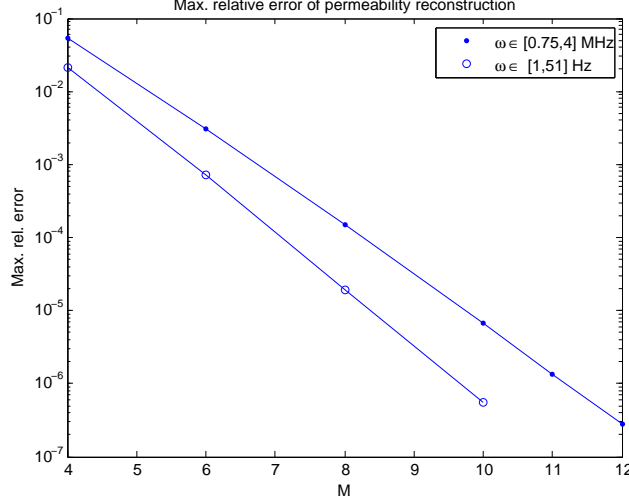


Figure 4: $E_\infty(P_{est}^M)$ for $\omega \in [1, 51]$ Hz and $\omega \in [0.75, 4]$ MHz.

Definition 5.1. [9] A function $g : (0, \infty) \rightarrow [0, \infty)$ is in \mathcal{S} if it can be represented as follows

$$g(\zeta) = a + \int_0^\infty \frac{d\sigma(t)}{\zeta + t}, \quad \zeta > 0$$

with constant $a \geq 0$ and a positive measure $d\sigma$ on $[0, \infty)$.

Let $\zeta := -\xi$ and $g(\zeta) := -R(\xi)$, which is well-defined for all $\zeta > 0$ because all the singularities of $R(\xi)$ are confined in $\xi \in [0, \Theta_1]$. Hence $g(\zeta) \in \mathcal{S}$ with $a = 0$ and $d\sigma = d\lambda$. It is known [9] that $\frac{1}{\zeta g(\zeta)} \in \mathcal{S}$ if $g(\zeta) \in \mathcal{S}$, therefore

$$\frac{\alpha_\infty}{\zeta g(\zeta)} = \frac{\alpha_\infty}{\xi R(\xi)} = a + \int_0^\infty \frac{d\sigma(t)}{-\xi + t} \text{ for some } a \geq 0 \text{ and positive measure } d\sigma, \zeta > 0$$

Since every function in \mathcal{S} can be analytically extended to the cut complex plane and $R(\xi)$ is analytic in $\mathbb{C} \setminus [0, \Theta_1]$, the expression above is valid in $\mathbb{C} \setminus [0, \Theta_1]$ and we conclude from (44) that the tortuosity function $T(\omega)$ has the following IRF:

Theorem 5.1. The dynamic tortuosity $T(\omega)$ has the following integral representation formula for ω such that $-\frac{i}{\omega} \in \mathbb{C} \setminus [0, \Theta_1]$

$$T(\omega) = a \left(\frac{i}{\omega} \right) + \int_0^{\Theta_1} \frac{d\sigma(t)}{1 - i\omega t} \quad (45)$$

for some constant $a \geq 0$ and positive measure $d\sigma$.

According to (3), $T(\omega)$ has a pole at $\omega = 0$ with strength $\frac{i\eta\phi}{\rho_f K_0}$, hence the a in (45) is

$$a = \frac{\eta\phi}{\rho_f K_0} = \frac{\alpha_\infty}{C_2}$$

Furthermore, $T(\omega) \rightarrow \alpha_\infty$ as $\omega \rightarrow \infty$, so $d\sigma$ has a Dirac mass at $t = 0$ with strength α_∞ . It is also interesting to note that (45) implies

$$\mu_0(d\sigma) = \frac{\nu^2 \phi}{K_0^2 F} \mu_1(d\lambda) = \frac{\phi F}{\mu_0^2(d\lambda)} \mu_1(d\lambda) = \frac{\alpha_\infty}{\mu_0^2(d\lambda)} \mu_1(d\lambda) \quad (46)$$

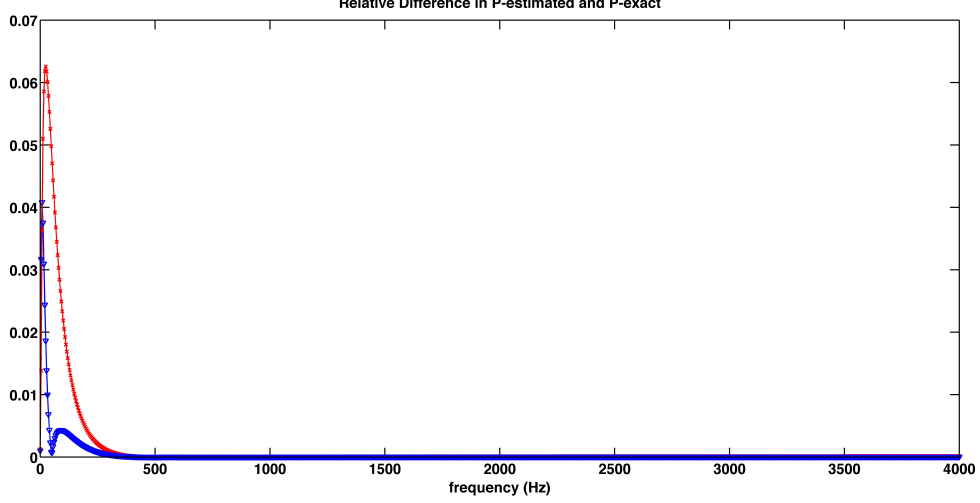


Figure 5: Comparison of relative error of P_{est}^{10} for different spacings of sample points. The red curve with crosses is from equally spaced sample points. The blue curve with triangles is from the modified approach.

which can be easily seen by taking the limit $\lim_{\omega \rightarrow 0} T(\omega) - \frac{ia}{\omega}$.

Suppose we have the data of $R(\xi_j)$, $\xi_j := -\frac{i}{\omega_j}$, $j = 1, \dots, M$ at different nonzero frequencies $\omega_j \in \mathbb{R}$, which can come from measurements of $K(\omega_j)$ or $T(\omega_j)$. To reconstruct $T(\omega)$, we first recognize that

$$h(\xi) := a - \frac{\alpha_\infty}{\xi R(\xi)} = a + i\omega T(\omega)$$

is a Stieltjes function with the symmetry $h(-\xi) = \overline{h(\xi)}$ for $\xi = -\frac{i}{\omega}$ and $\omega \in \mathbb{R}$, i.e. measurement at M different non-zero frequencies provide $2M$ data. Similar with Section 4, we can use these $2M$ data points to reconstruct $h(\xi)$ by using multipoint Padé approximants

$$h(\xi_j) = \int_0^{\Theta_1} \frac{d\sigma(\Theta)}{\xi_j - \Theta} \approx [M - 1/M]_h(\xi_j) := \frac{a_0 + a_1\xi_j + \dots + a_{M-1}\xi_j^{M-1}}{1 + b_1\xi_j + \dots + b_M\xi_j^M}, \quad j = 1, 2, \dots, 2M \quad (47)$$

Once the $[M - 1/M]_h(\xi)$ is known, its partial fraction decomposition can be numerically obtained

$$[M - 1/M]_h(\xi) = \sum_{j=1}^M \frac{r_j}{\xi - p_j}, \quad r_j > 0, 0 < p_j < \Theta_1 \quad (48)$$

and the dynamic tortuosity T can be approximated in terms of residues r_j and poles p_j , $j = 1, \dots, M$

$$T(\omega) \approx \frac{a}{-i\omega} + \sum_{j=1}^M \frac{r_j/p_j}{-i\omega + 1/p_j} \quad (49)$$

Therefore, the tortuosity in time domain can be approximated as

$$\mathcal{F}^{-1}[T](t) = a\delta(t) + \sum_{j=1}^M \left(\frac{r_j}{p_j} \right) e^{-\frac{t}{p_j}}, \quad t \geq 0. \quad (50)$$

with p_j and r_j defined in (48).

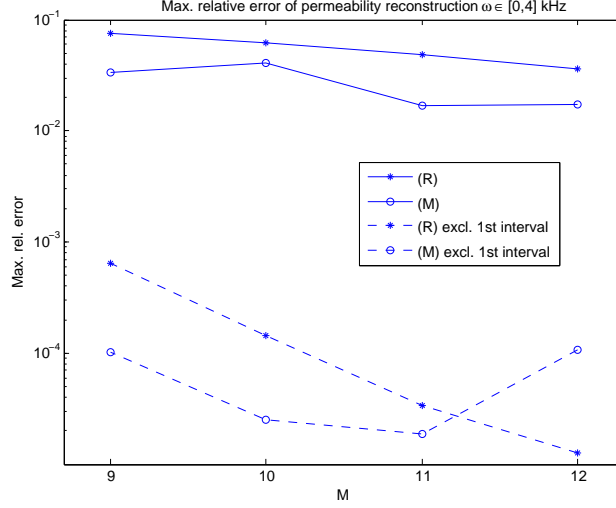


Figure 6: $E_\infty(P_{est}^M)$ for $\omega \in [0, 4]$ kHz. (R): equally spaced (M): Modified.

5.2 Formulation and Algorithm for $T(\omega)$

Given the permeability data $P(s_j)$, $s_j := -i\omega_j$, $j = 1, \dots, M$ at different nonzero frequencies $\omega_j \in \mathbb{R}$, we compute the data points for $D(s)$ defined as

$$D(s) := T(\omega) - \frac{ia}{\omega} = \frac{\alpha_\infty}{sP(s)} - \frac{a}{s} = \int_0^{\Theta_1} \frac{d\sigma(\Theta)}{1 + s\Theta} \quad (51)$$

Note that

$$\lim_{s \rightarrow 0} D(s) = \int_0^{\Theta_1} d\sigma(\Theta) < \infty.$$

Using symmetry, there are $2M$ data points for reconstructing $D(s)$ by multipoint Padé approximates

$$D(s_j) = \int_0^{\Theta_1} \frac{d\sigma(\Theta)}{1 + s_j\Theta} \approx [M - 1/M]_D(s) := \frac{a_0 + a_1 s_j + \dots + a_{M-1} s_j^{M-1}}{1 + b_1 s_j + \dots + b_M s_j^M}, \quad j = 1, 2, \dots, 2M \quad (52)$$

The linear system of a_0, \dots, a_M and b_1, \dots, b_M to be solved has the same structure as that in Section 4.1 except $P(s_j)$ and P_j in (29) should be replaced with $D(s_j)$ and D_j , respectively. The numerical scheme is identical to the 4-step process described in Section 4.1.

Once the $[M - 1/M]_D(s)$ is known, its partial fraction decomposition can be numerically obtained

$$[M - 1/M]_D(s) = \sum_{j=1}^M \frac{r_j}{s - p_j}, \quad r_j > 0, p_j \in (-\infty, -\frac{1}{\Theta_1}) \quad (53)$$

and the dynamic tortuosity T can be approximated in terms of the residues and poles of $[M - 1/M]_D(s)$

$$T(\omega) \approx \frac{a}{-i\omega} + \sum_{j=1}^M \frac{r_j}{-i\omega - p_j}$$

Therefore, the tortuosity in time domain can be expressed as

$$\mathcal{F}^{-1}[T](t) = a\delta(t) + \sum_{j=1}^M r_j e^{p_j t} \quad (54)$$

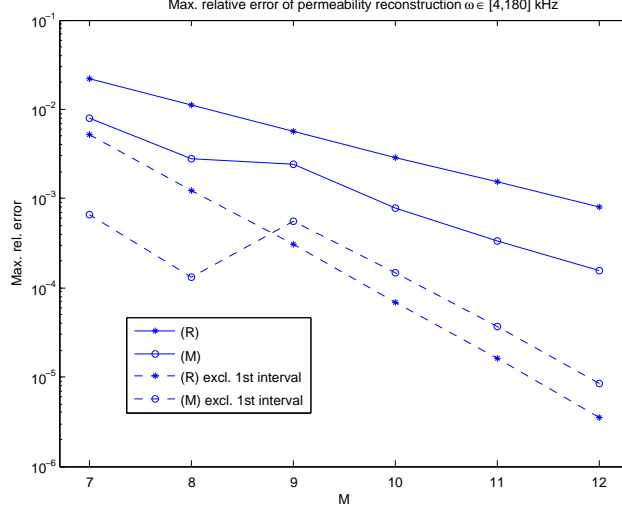


Figure 7: $E_\infty(P_{est}^M)$ for $\omega \in [4, 180]$ kHz. (R): equally spaced (M): Modified.

where $r_j > 0$ and $p_j < 0$ are defined in (53) and $\delta(t)$ is the Dirac function.

We use the JKD tortuosity function to demonstrate the idea.

5.3 Numerical Results for JKD tortuosity $T^D(\omega)$

The function corresponding to T^D via (51) is

$$D^D(s) := \frac{\alpha_\infty}{sP^D(s)} - \frac{a}{s} = \alpha_\infty + \frac{\alpha_\infty(\sqrt{1+C_1s}-1)}{C_2s} = \int_0^{\Theta_1} \frac{d\sigma^D(\Theta)}{1+s\Theta} \quad (55)$$

We use the values of parameters in Table 2 for the simulations. For these parameters, $a = \frac{\eta\phi}{\rho_f K_0} = 2.708895e03$.

Suppose M' poles are retained after the algorithm, $M' \leq M$, we reindex them and the corresponding residues to $\{(p_j, r_j)\}_{j=1}^{M'}$. The function $D(s)$ is then approximated by

$$D(s) \approx D_{est}^M(s) := \sum_{j=1}^{M'} \frac{r_j}{s-p_j} = \sum_{j=1}^{M'} \frac{r_j}{s-p_j} = \sum_{j=1}^{M'} \frac{-r_j/p_j}{1+s(-1/p_j)} \quad (56)$$

and the moments $\mu_k(d\sigma^D)$, $k = 0, 1, 2, \dots$ by

$$\mu_k(d\sigma^D) \approx (-1)^{k+1} \sum_{j=1}^{M'} \frac{r_j}{(p_j)^{k+1}}. \quad (57)$$

In terms of the poles and residues in (56), the time domain tortuosity T can be approximated as

$$\mathcal{F}^{-1}\{T\}(t) \approx \frac{\eta\phi}{\rho_f K_0} \delta(t) + \sum_{j=1}^{M'} r_j e^{p_j t}, \quad r_j > 0, \quad p_j < 0.$$

We consider the same frequency ranges as in Section 4.3. Table 4 shows the reconstructed moments of $d\sigma^D$ from data in the frequency range from 1 to 51 Hz with multipoint Padé approximants of various order M ; the plot is demonstrated in Figure 8. The exact values of moments

are computed by first observing that D^D has a removable singularity at $s = 0$ and its Taylor expansion near $s = 0$ can be explicitly expressed as

$$D^D(s) = \sum_{k=0}^{\infty} c_k s^k$$

with

$$c_0 = \alpha_{\infty} + \frac{2K_0\alpha_{\infty}^2}{\phi\Lambda^2} \text{ and } c_k = \frac{(-1)^k C_1^{k+1} \alpha_{\infty}}{(k+1)! 2^{k+1} C_2} \prod_{j=1}^k (2j-1), \quad k \geq 1$$

Differentiating the IRF in (55) with respect to s and compare both sides, we can express the moments of $d\sigma^D$ in terms of the Taylor coefficients of D^D near $s = 0$

$$\mu_k(d\sigma^D) = (-1)^k c_k, \quad k = 0, 1, 2, \dots \quad (58)$$

Table 4: Moments of $d\sigma^D$ constructed from data in $[1, 51]\text{Hz}$

	Exact	$M=9$	$M=7$	$M=5$	$M=3$
M'		8	6	4	2
μ_0	0.2448054 e3	0.2448050 e3	0.2447906 e3	0.2442974 e3	0.2313087 e3
μ_1	0.1096426 e2	0.1096420 e2	0.1096153 e0	0.1088098 e2	0.9286772 e1
μ_2	0.9864792 e0	0.9864178 e0	0.9844351 e0	0.9460585 e0	0.5683834 e0
μ_3	0.1109447 e0	0.1109081 e0	0.1100577 e0	0.9890620 e-1	0.3758564 e-1
μ_4	0.1397472 e-1	0.1395836 e-1	0.1367750 e-1	0.1108704 e-1	0.2511712 e-2
μ_5	0.1886006 e-2	0.1879998 e-2	0.1801971 e-2	0.1278614 e-2	0.1680769 e-3
μ_6	0.2666530 e-3	0.2647426 e-3	0.2455669 e-3	0.1491975 e-3	0.1124921 e-4
μ_7	0.3898596 e-4	0.3844154 e-4	0.3413699 e-4	0.1749433 e-4	0.7529144 e-6
μ_8	0.5846091 e-5	0.5703658 e-5	0.4801441 e-5	0.2055462 e-5	0.5039304 e-7
μ_9	0.8941761 e-6	0.8593632 e-6	0.6800106 e-6	0.2417042 e-6	0.3372839 e-8

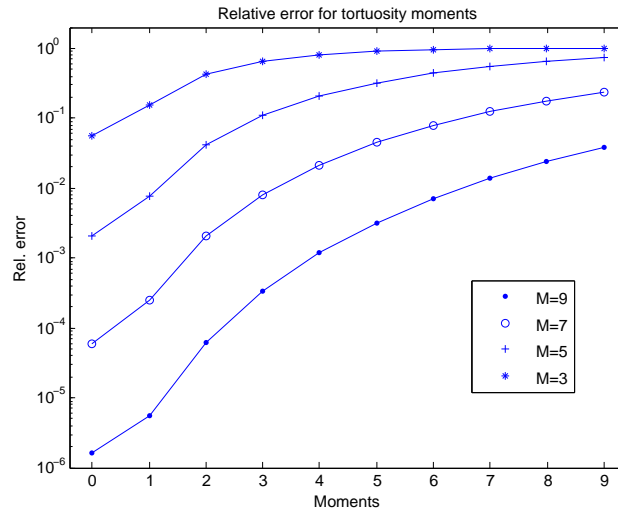


Figure 8: . Relative error of $\mu_1(d\sigma^D), \dots, \mu_9(d\sigma^D)$ approximated from M data points

Due to the important roles played by the poles and residues in handling the memory terms in Biot-JKD equations, we list $\{p_j, r_j\}_{j=1}^{M'}$ for $M = 9$ and $M = 7$ in Table 5 with $j = 1, \dots, M'$. The maximum relative error of D_{est}^M is defined as

Table 5: Poles and residues of $[M - 1/M]_{DD}(s)$ constructed from data in $[1, 51]\text{Hz}$,

	$M = 9$		$M = 7$	
	p_j	r_j	p_j	r_j
$j = 1$	-1.706303 e3	6.240356 e4	-9.475742 e2	4.524730 e4
$j = 2$	-1.988249 e2	6.285370 e3	-1.183222 e2	4.649229 e3
$j = 3$	-7.810948 e1	2.285702 e3	-4.647002 e1	1.807574 e3
$j = 4$	-4.120607 e1	1.252540 e3	-2.284838 e1	1.018569 e3
$j = 5$	-2.398527 e1	8.133531 e1	-1.199244 e1	5.693354 e2
$j = 6$	-1.450089 e1	5.338794 e1	-6.992178 e0	1.873584 e2
$j = 7$	-9.133035 e0	2.945426 e1		
$j = 8$	-6.391875 e0	8.937405 e0		

$$E_\infty(D_{est}^M) := \max_{s \in [-i\omega_{min}, -i\omega_{max}]} \frac{|D(s) - D_{est}^M|}{|D(s)|}$$

and evaluated the same way as that of P_{set}^M in Section 4.3. The maximum relative error for frequency range $[1, 51]\text{Hz}$ and $[0.75, 4]\text{ MHz}$, $[0, 4000]\text{Hz}$ and $[4, 180]\text{ kHz}$ are listed in Figures 9, 10 and 11, respectively.

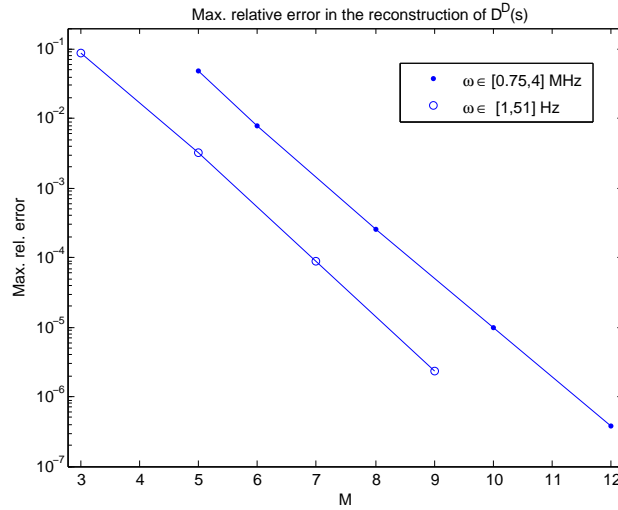


Figure 9: . $E_\infty(D_{est}^M)$ for $\omega \in [1, 51]\text{ Hz}$ and $\omega \in [0.75, 4]\text{ MHz}$

6 Remarks on the relation between moments and various effective parameters

Using the IRFs, we can derive several relations between the moments of $d\lambda$, $d\sigma$ and various combinations of dynamic effective parameters. Recall that $d\lambda$ corresponds to the permeability

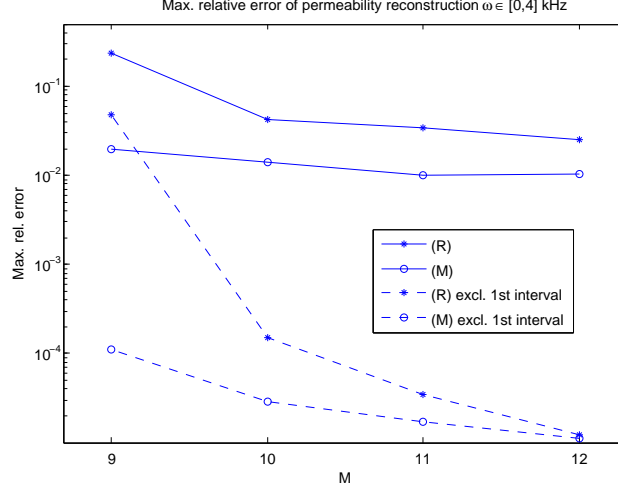


Figure 10: $E_\infty(D_{est}^M)$ for $\omega \in [0, 4]$ kHz. (R): equally spaced (M): Modified.

function and $d\sigma$ to the tortuosity function. Since the dynamic permeability and dynamic tortuosity depend on both the frequency and the pore space geometry, the fact that the integrands in the IRFs are only functions of frequency implies that all the geometrical information must be encoded in the measures. The analyticity of both functions at $s = 0$ enable the calculation of moments in terms of the coefficients of Taylor expansions there. For example, (22) implies

$$\mu_0(d\lambda) = \frac{FK_0}{\nu} = \frac{\alpha_\infty K_0}{\phi\nu} \quad (59)$$

The relation between the permeability and the tortuosity leads to the following relation between the moments of $d\lambda$ and $d\sigma$

$$\mu_p(d\lambda) = \frac{\mu_0(d\lambda)}{\alpha_\infty} \sum_{k+j=p-1} \mu_k(d\sigma) \mu_j(d\lambda), \quad p \geq 1 \quad (60)$$

From (60), the infinite-frequency α_∞ can be expressed in terms of moments

$$\alpha_\infty = \frac{\mu_0(d\sigma)\mu_0^2(d\lambda)}{\mu_1(d\lambda)} \quad (61)$$

For the JKd permeability and tortuosity, the measure $d\sigma^D$ satisfies

$$\mu_0(d\sigma^D) = \int_0^{\Theta_1} d\sigma^D(\Theta) = \lim_{s \rightarrow 0} D^D(s) = \alpha_\infty + \frac{2K_0\alpha_\infty^2}{\phi\Lambda^2} \quad (62)$$

Suppose we can reconstruct $\mu_0(d\lambda^D)$ and $\mu_0(d\sigma^D)$ from low frequency data of permeability $K(\omega)$ and that we know the porosity ϕ and pore fluid kinetic viscosity ν , then we can recover α_∞ from the fact that $\mu_0(d\lambda^D) = \frac{\alpha_\infty K_0}{\phi\nu}$ because K_0 can be obtained easily through extrapolation of low frequency data. Once α_∞ is known, (62) can be used to recover Λ , which is a weighted pore volume-to-surface ratio that provides a measure of the dynamically connected part of the pore region [7]. We note that (62) implies the following for the JKD model

$$\Lambda = \sqrt{\frac{2K_0\alpha_\infty^2}{\phi[\mu_0(d\sigma^D) - \alpha_\infty]}} = \sqrt{\frac{2K_0\alpha_\infty}{\phi[\frac{\mu_1(d\lambda^D)}{\mu_0^2(d\lambda^D)} - 1]}} \quad (63)$$

Formulas (59), (61) and (63) show exactly how microstructural information affects the effective parameters α_∞ and Λ through moments.

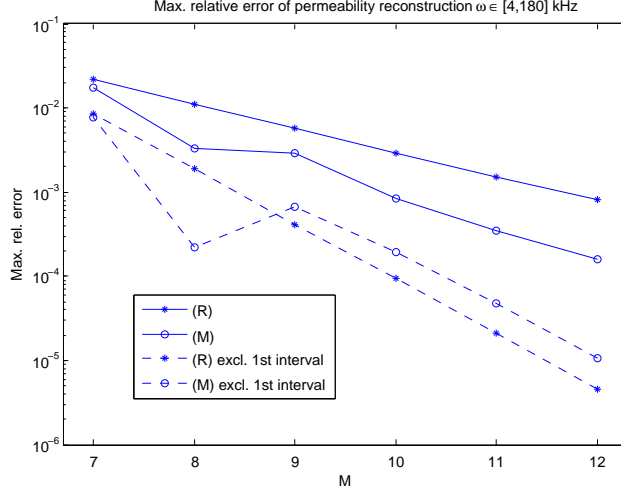


Figure 11: $E_{\infty}(D_{est}^M)$ for $\omega \in [4, 180]$ kHz. (R): equally spaced (M): Modified.

7 Conclusion

In this paper, we derived the integral representation formula (IRF) for dynamic tortuosity $T(\omega)$ in general form; we show that $T(\omega)$ can be written as the sum of a function with a simple pole at 0 and a Stieltjes function. Utilizing the analytic structure of this IRF and the IRF of permeability $K(\omega)$ derived in [7], an algorithm based on multipoint Padé approximation of Stieltjes functions is proposed for constructing $K(\omega)$ and $T(\omega)$ from the values of permeability at district frequencies. Taking into account the symmetry of Stieltjes functions, only M different frequencies, instead of $2M$, are needed for constructing the $[M - 1/M]$ approximant. It is demonstrated that the moments of both the measures in the IRFs of $K(\omega)$ and $T(\omega)$ can be estimated to high accuracy from low frequency data. The capability of this algorithm for recovering the moments can be utilized to compute the inf-tortuosity α_{∞} through (59) using the low-frequency permeability data, if the viscosity of pore fluid ν is known because K_0 can be approximated very well from $P_{est}^M(s)$.

Furthermore, if the JKD model is used, the microstructure-dependent parameter Λ can be recovered by the formula in (63). It is interesting to note that the empirical formula for Λ suggested by JKD [54] is $\Lambda \approx \sqrt{\frac{2\alpha_{\infty}K_0}{\phi/4}}$. Comparing this with (63), which is exact, this empirical formula corresponds to the assumption that $\frac{\mu_1(d\lambda^D)}{\mu_0^2(d\lambda^D)} = \frac{5}{4}$, which is not always true and obviously not satisfied by the moments calculated in this paper.

We have also shown that the JKD permeability $K^D(\omega)$ can indeed be represented by a probability measure in its IRF, as is predicted by the general result in [7].

The results of numerical experiments conducted on the frequency ranges taken from the literature in biomechanics for bone [59] and seismology [47] are presented. For the bandwidth spreading less than two orders of magnitude, the proposed algorithm with equally spacing interpolating points achieve approximates with high accuracy. From the last two numerical examples, we see that the approximation is of good accuracy away from the first interval; the max. relative error can be greatly improved by adding one sample point close to the lowest frequency to the equally spaced points. This implies that the location of sample points play an important role in the approximation and will be the topic of future investigation. Another

way to handle wide frequency range can be to divide it into shorter intervals and do local approximation. The advantage of our reconstruction scheme is two-fold. First of all, it provides high accuracy interpolation of the permeability/tortuosity data without assuming anything beyond the fact that they are related to Stieltjes functions and hence is more general than the JKD model, which assumes specific forms of the dynamic tortuosity functions. Secondly, the time domain representation such as (54) provides an efficient way for numerically handling the memory terms that appears in the time domain numerical simulation for wave propagation in poroelastic materials.

Acknowledgement: This research is partially sponsored by ARRA-NSF-DMS Math. Biology Grant 0920852.

References

- [1] Mark J Ablowitz and Athanassios S Fokas. *Complex variables: Introduction and applications*. Cambridge University Press, 2003.
- [2] Naum Il'ich Akhiezer and Izrail Markovich Glazman. *Theory of linear operators in Hilbert space*, volume 1. Dover publications, 1993.
- [3] Jean F Allard, Bernard Castagnede, Michel Henry, and Walter Lauriks. Evaluation of tortuosity in acoustic porous materials saturated by air. *Review of scientific instruments*, 65(3):754–755, 1994.
- [4] Keith Attenborough, David L. Berry, and Yu Chen. Acoustic scattering by near-surface inhomogeneities in porous media. Technical report, Defense Technical Information Center OAI-PMH Repository [<http://stinet.dtic.mil/oai/oai>] (United States), 1998.
- [5] JL Auriault. Dynamic behaviour of a porous medium saturated by a newtonian fluid. *International Journal of Engineering Science*, 18(6):775–785, 1980.
- [6] J.L. Auriault, L. Borne, and R. Chambon. Dynamics of porous saturated media, checking of the generalized law of Darcy. *The Journal of the Acoustical Society of America*, 77:1641, 1985.
- [7] M. Avellaneda and S. Torquato. Rigorous link between fluid permeability, electrical conductivity, and relaxation times for transport in porous media. *Physics of Fluids A: Fluid Dynamics*, 3:2529, 1991.
- [8] G.A. Baker and P. Graves-Morris. *Padé approximants (Chapter 5)*, volume 59. Cambridge University Press, 1996.
- [9] Christian Berg. *Quelques remarques sur le cône de Stieltjes in Séminaire de théorie du potentiel*, volume 814 of *Lecture notes in Mathematics*, pages 70–79. Springer, Paris, 1980.
- [10] M.A. Biot. Theory of propagation of elastic waves in a fluid-saturated porous solid. I. Low-frequency range. *The Journal of the Acoustical Society of America*, 28:168, 1956.
- [11] M.A. Biot. Theory of propagation of elastic waves in a fluid-saturated porous solid. II. Higher frequency range. *The Journal of the Acoustical Society of America*, 28(2):179–191, 1956.
- [12] M.A. Biot. Mechanics of deformation and acoustic propagation in porous media. *Journal of applied physics*, 33(4):1482–1498, 1962.
- [13] J. L. Buchanan, R. P. Gilbert, A. Wirgin, and Y. S. Xu. *Marine acoustics: direct and inverse problems*. SIAM, Philadelphia, 2004.
- [14] James L. Buchanan and Robert P. Gilbert. Determination of the parameters of cancellous bone using high frequency acoustic measurements. *Mathematical and Computer Modelling*, 45:281–308, 2007.

- [15] James L. Buchanan, Robert P. Gilbert, and Khaldoun Khashanah. Determination of the parameters of cancellous bone using low frequency acoustic measurements. *Journal of Computational Acoustics*, 12(2):99–126, 2004.
- [16] J.L. Buchanan, R.P. Gilbert, and M. Y Ou. Recovery of the parameters of cancellous bone by inversion of effective velocities, and transmission and reflection coefficients. *Inverse Problems*, 27:125006, 2011.
- [17] R. Burridge and J.B. Keller. Poroelasticity equations derived from micro-structure. *J. Acoust. Soc. Am.*, 70:1140–1146, 1981.
- [18] J. M. Carcione, C. Morency, and J. E. Santos. Computational poroelasticity – a review. *Geophysics*, 75(5):75A229–75A243, 2010.
- [19] J.M. Carcione. Wave propagation in anisotropic, saturated porous media: Plane-wave theory and numerical simulation. *The Journal of the Acoustical Society of America*, 99(5):2655–2666, 1996.
- [20] J.M. Carcione. *Wave Fields in Real Media: Wave Propagation in Anisotropic, Anelastic and Porous Media*. Pergamon-Elsevier, Oxford, 2001.
- [21] E. Cherkaev and M.J.Y. Ou. Dehomogenization: reconstruction of moments of the spectral measure of the composite. *Inverse Problems*, 24(6):065008, 2008.
- [22] G. Chiavassa and B. Lombard. Time domain numerical modeling of wave propagation in 2D heterogeneous porous media. *Journal of Computational Physics*, 230(13):5288–5309, 2011.
- [23] T. Clopeau, J.L.Ferrín, R. P. Gilbert, , and A. Mikelić. Homogenizing the acoustic properties of the seabed, part ii. *Mathematical and Computer Modelling*, 33:821–841, 2001.
- [24] S. C. Cowin. Bone poroelasticity. *Journal of Biomechanics*, 32:27–238, 1999.
- [25] S. C. Cowin and L. Cardoso. Fabric dependence of bone ultrasound. *Acta of Bioengineering and Biomechanics*, 12(2), 2010.
- [26] N. Dai, A. Vafidis, and E. Kanasewich. Wave propagation in heterogeneous porous media: a velocity-stress, finite-difference method. *Geophysics*, 60:327–340, 1995.
- [27] J. de la Puente, M. Dumbser, M. Käser, and H. Igel. Discontinuous Galerkin methods for wave propagation in poroelastic media. *Geophysics*, 73(5):T77–T97, 2008.
- [28] G. Degrande and G. De Roeck. FFT-based spectral analysis methodology for one-dimensional wave propagation in poroelastic media. *Transport in Porous Media*, 9:85–97, 1992.
- [29] E. Detournay and A. H-D. Cheng. Poroelastic response of a borehole in a non-hydrostatic stress field. *International Journal of Rock Mechanics and Mining Sciences and Geomechanics Abstracts*, 25(3):171–182, 1988.
- [30] Geoffrey Dougherty and Jozsef Varro. A quantitative index for the measurement of the tortuosity of blood vessels. *Medical engineering & physics*, 22(8):567–574, 2000.
- [31] Tyler DuBeshter, Puneet K Sinha, Alex Sakars, Gerald W Fly, and Jacob Jorne. Measurement of tortuosity and porosity of porous battery electrodes. *Journal of The Electrochemical Society*, 161(4):A599–A605, 2014.
- [32] Z.E.A. Fellah, J.Y. Chapelon, S. Berger, W. Lauriks, and C. Depollier. Ultrasonic wave propagation in human cancellous bone: Application of the Biot theory. *J. Acoust. Soc. Am.*, 116(1):61–73, 2004.
- [33] S. K. Garg, A. H. Nayfeh, and A. J. Good. Compressional waves in fluid-saturated elastic porous media. *Journal of Applied Physics*, 45:1968–1974, 1974.

- [34] Jan Gelfgren. Rational interpolation to functions of Stieltjes' type. Technical report, Department of Mathematics, University of Umeå, 1978.
- [35] R. P. Gilbert, P. Guyenne, and M. Yvonne Ou. A quantitative ultrasound model of the bone with blood as the interstitial fluid. *Mathematical and Computer Modelling*, 55:2029–2039, 2012.
- [36] R. P. Gilbert and Z. Lin. Acoustic field in a shallow, stratified ocean with a poro-elastic seabed. *Zeitschrift für Angewandte Mathematik und Mechanik*, 77(9):677–688, 1997.
- [37] R. P. Gilbert and M. Yvonne Ou. Acoustic wave propagation in a composite of two different poroelastic materials with a very rough periodic interface: a homogenization approach. *International Journal for Multiscale Computational Engineering*, 1(4), 2003.
- [38] RP Gilbert and A Mikelić. Homogenizing the acoustic properties of the seabed: Part i. *Nonlinear Analysis: Theory, Methods & Applications*, 40(1):185–212, 2000.
- [39] Per Christian Hansen and Dianne Prost O'Leary. The use of the L-curve in the regularization of discrete ill-posed problems. *SIAM Journal on Scientific Computing*, 14(6):1487–1503, 1993.
- [40] S. Hassanzadeh. Acoustic modeling in fluid-saturated porous media. *Geophysics*, 56:424–435, 1991.
- [41] A. Hosokawa and T. Otani. Ultrasonic wave propagation in bovine cancellous bone. *The Journal of the Acoustical Society of America*, 101:558, 1997.
- [42] E.R. Hughes, T.G. Leighton, P.R. White, and G.W. Petley. Investigation of an anisotropic tortuosity in a biot model of ultrasonic propagation in cancellous bone. *The Journal of the Acoustical Society of America*, 121:568, 2007.
- [43] D.L. Johnson, J. Koplik, and R. Dashen. Theory of dynamic permeability and tortuosity in fluid-saturated porous media. *Journal of fluid mechanics*, 176(1):379–402, 1987.
- [44] D.L. Johnson, T.N. McAllister, and J.A. Frangos. Fluid flow stimulates rapid and continuous release of nitric oxide in osteoblasts. *American Journal of Physiology-Endocrinology And Metabolism*, 271(1):E205–E208, 1996.
- [45] G.I. Lemoine, M.Y. Ou, and R.J. LeVeque. High-resolution finite volume modeling of wave propagation in orthotropic poroelastic media. *SIAM Journal on Scientific Computing*, 35(1):B176–206, 2013.
- [46] Grady Lemoine and M. Yvonne Ou. Finite volume modeling of poroelastic-fluid wave propagation with mapped grids. *SIAM Journal on Scientific Computing*, to appear, 2013.
- [47] Jian-Fei Lu and Andrzej Hanyga. Wave field simulation for heterogeneous porous media with singular memory drag force. *Journal of Computational Physics*, 208(2):651–674, 2005.
- [48] Maciej Matyka and Zbigniew Koza. How to calculate tortuosity easily? *arXiv preprint arXiv:1203.5646*, 2012.
- [49] TN McAllister and JA Frangos. Steady and transient fluid shear stress stimulate no release in osteoblasts through distinct biochemical pathways. *Journal of Bone and Mineral Research*, 14(6):930–936, 1999.
- [50] B. G. Mikhailenko. Numerical experiment in seismic investigations. *Journal of Geophysics*, 58:101–124, 1985.
- [51] C. Morency and J. Tromp. Spectral-element simulations of wave propagation in porous media. *Geophysical Journal International*, 179:1148–1168, 2008.
- [52] M.J.Y. Ou. On nonstandard pade approximants suitable for effective properties of two-phase composite materials. *Applicable Analysis*, 91(1):173–187, 2012.

- [53] I. Owan, D.B. Burr, C.H. Turner, J. Qiu, Y. Tu, J.E. Onyia, and R.L. Duncan. Mechanotransduction in bone: osteoblasts are more responsive to fluid forces than mechanical strain. *American Journal of Physiology-Cell Physiology*, 273(3):C810–C815, 1997.
- [54] Steve Pride. Modeling the drag forces of porous media acoustics. Technical report, Massachusetts Institute of Technology. Earth Resources Laboratory, 1992.
- [55] K.M. Reich and J.A. Frangos. Effect of flow on prostaglandin E2 and inositol trisphosphate levels in osteoblasts. *American Journal of Physiology-Cell Physiology*, 261(3):C428–C432, 1991.
- [56] A.G. Robling, A.B. Castillo, and C.H. Turner. Biomechanical and molecular regulation of bone remodeling. *Annu. Rev. Biomed. Eng.*, 8:455–498, 2006.
- [57] K. Sakai, M. Mohtai, and Y. Iwamoto. Fluid shear stress increases transforming growth factor beta 1 expression in human osteoblast-like cells: modulation by cation channel blockades. *Calcified tissue international*, 63(6):515–520, 1998.
- [58] J. E. Santos and E. J. Oreña. Elastic wave propagation in fluid-saturate porous media, part II: The Galerkin procedures. *Mathematical Modeling and Numerical Analysis*, 20:129–139, 1986.
- [59] N. Sebaa, Z. E. A. Fellah, M. Fellah, E. Ogam, A. Wirgin, F. G. Mitri, C. Depollier, and W. Lauriks. Ultrasonic characterization of human cancellous bone using the biot theory: Inverse problem. *J. Acoust. Soc. Am.*, 120(4):1816–1824, 2006.
- [60] RE Showalter. Diffusion in poro-elastic media. *Journal of Mathematical Analysis and Applications*, 251(1):310–340, 2000.
- [61] Baorui Song and Hua Lian. Convergence of the rational interpolants of stieltjes functions. *Journal of computational and applied mathematics*, 159(1):129–135, 2003.
- [62] M F Souzanchi, P E Palacio Mancheno, Y Borisov, L Cardoso, and SC Cowin. Tortuosity and the averaging of micro-velocity fields in poroelasticity. *Journal of Applied Mechanics (to appear)*, 2012.
- [63] Rahul Vallabh, Pamela Banks-Lee, and Abdel-Fattah Seyam. New approach for determining tortuosity in fibrous porous media. *Journal of Engineered Fabrics & Fibers (JEFF)*, 5(3), 2010.
- [64] DK Wilson. Simple, relaxational models for the acoustical properties of porous media. *Applied Acoustics*, 50(3):171–188, 1997.
- [65] D. Zhang. *Inverse electromagnetic problem for microstructured media*. PhD thesis, Dept. of Mathematics, University of Utah, 2007.
- [66] D. Zhang and E. Cherkaev. Reconstruction of spectral function from effective permittivity of a composite material using rational function approximations. *Journal of Computational Physics*, 228(15):5390–5409, 2009.
- [67] Min-Yao Zhou and Ping Shen. First-principles calculations of dynamic permeability in porous media. *Physical Review B*, 39(16):12027–12039, 1989.